Effect of temperature and incident ion energy on nanostructure formation on silicon exposed to helium plasma

*Matt Thompson[1], Shi Quan[2], Shin Kajita[2], Noriyasu Ohno[2], Cormac Corr[1]

[1] Department of Electronic Materials Engineering, Research School of Physics, Australian National University, Canberra, Australia

[2] Graduate School of Engineering, Nagoya University, Nagoya 464-8603, Japan

*Corresponding Author email: matt.a.thompson@anu.edu.au

Abstract

Helium plasma can be used to deliver low energy (<100 eV) helium ions to stimulate the growth of nanostructures on silicon surfaces. This can produce a wide range of surface features including nanoscale roughening, nanowires and porous structures. Nanostructure sizes varied from ~ 10 nm to over 100 nm in diameter. The effect of these structures on surface reflectivity for photovoltaic and photocatalytic applications is also investigated. Broad-band suppression of photo-reflectivity is achieved across the 300-1200 nm wavelength range studied for silicon exposed to helium plasma at 600 °C, with an average reflectivity of 3.2% and 2.9% for incident helium ion energies of 42 eV and 62 eV, respectively.

1. Introduction

Nanostructures provide exciting opportunities for the development of new materials that can have radically different properties to their bulk counterparts. Quantum confinement effects that emerge at the nano-scale significantly alter electronic band structures in a size-dependent manner, which can be exploited to tune the optical[1–3], electronic[4,5], and catalytic properties[6,7] of a target material. The inherently high surface area of many nanostructures (such as wires[8,9] and porous meshes[10]) also make them attractive candidates for high-performance catalysts[11], fuel cell[12] and battery electrodes[13], and high-sensitivity chemical sensors[14]. Nanostructures can also be used to change other properties, such as changing surface geometry to suppress reflection[15,16], or light-triggered dissolution within biological media[17].

The great diversity of nanostructures and their applications is matched by a tremendous diversity of processes through which they can be created. Here, we focus our attention on a process which utilizes a high-flux helium plasma to induce the growth of fine nano-scale surface features in a wide range of materials, including tungsten[18,19], platinum[20], silicon[21,22] and germanium[23]. This process is attractive as it eliminates the need for complex chemical precursors or catalytic seeds that are widely used in other bottom-up fabrication processes.

The helium-plasma process is interesting as limited chemical interaction occurs between the helium plasma and target material, suggesting the nanostructures are produced through some combination of sputtering, atomic (re)deposition, surface adatom kinetics, and the dynamics of vacancy-helium clusters[19,23]. Though the nanostructure formation regime has been widely studied in tungsten in the context of nuclear fusion research, where nano-scale structures can lead to enhanced degradation of reactor walls[24–26], the specifics of the nanostructure growth process are not fully understood.

In this work, the effect of substrate temperature (450 °C – 700 °C) and incident helium ion energy on nanostructure formation in silicon is explored using pure helium plasma in the high-flux NAGDIS-II linear plasma device. The nanostructure growth is significantly influenced by the plasma exposure

conditions. Wire-like structures are observed to grow under most conditions, with the packing density of nanowires decreasing and their size increasing with increasing temperature. Under certain conditions a novel wool-like morphology was observed which appears to be a network composed of fine (~10 nm diameter) interconnected wires. Photo-reflectivity measurements reveal a significant drop in the reflectivity of surfaces coated with these structures across the visible and near-infrared spectrum, highlighting the potential to use helium-processing to enhance the light absorption of silicon photoelectric and photocatalytic cells.

2. Experimental procedure

Polished single crystal silicon samples with a (100) surface orientation were exposed to a helium plasma in the high-flux NAGDIS-II linear plasma device[27]. NAGDIS-II generates plasma via a high-density DC plasma discharge in the source region where charged particles are radially confined via external magnetic fields as the plasma diffuses downstream to the water-cooled sample holder. Silicon samples were doped with boron to reduce the electrical resistivity to $\leq$ 0.005 ohm-cm to ensure good electrical contact through the plasma, sample, and sample holder. The sample temperature was measured with a KTL-PRO pyrometer, and held at a constant temperature between 450 °C and 700 °C over the course of the exposure for a total of 1800 seconds assuming a constant emissivity of 0.4. This temperature range was selected as it is known from past work to produce well-formed nanostructures[23]. Temperature measurements were taken early in the exposure, prior to any significant nanostructure formation. Due to the very high heat fluxes in NAGDIS-II sample heating was achieved solely through plasma heating. The temperature was varied by changing the DC current through the plasma and inserting spacers behind the silicon samples to reduce thermal conductivity to the water-cooled sample holder.

Samples were negatively biased with an external power supply in order to vary the incident energy of positively-charged helium ions from 19 eV to 65 eV. The ion flux and floating potential were calculated using a reciprocating electrostatic probe located 30 cm upstream from the sample holder position. Incident ion energy was approximated as the difference between the sheath potential and the bias potential of the external power supply. Bias potentials were fixed at -40 V, -60 V, or -80 V to provide "low", "intermediate" or "high" energy incident ions. The incident ion flux varied between $7 \times 10^{21}\mathrm{He} \cdot \mathrm{m}^{-2}s^{-1}$ and $2.5 \times 10^{22}\ \mathrm{He} \cdot \mathrm{m}^{-2}\mathrm{s}^{-1}$ between different exposures. The flux could be varied by varying the DC current through the plasma source. A schematic of the NAGDIS-II device is presented in Figure 1.

After exposure sample surfaces were imaged via the through-lens secondary electron detector of a Zeiss UltraPlus FESEM at the ANU's Centre of Advanced Microscopy. Areal densities and nanostructure sizes were estimated using the ImageJ v. 1.52a software package[28]. Surface reflectivity measurements were performed on a PerkinElmer Lambda 1050 spectrophotometer over a wavelength range from 300 nm to 1200 nm in 10 nm steps.

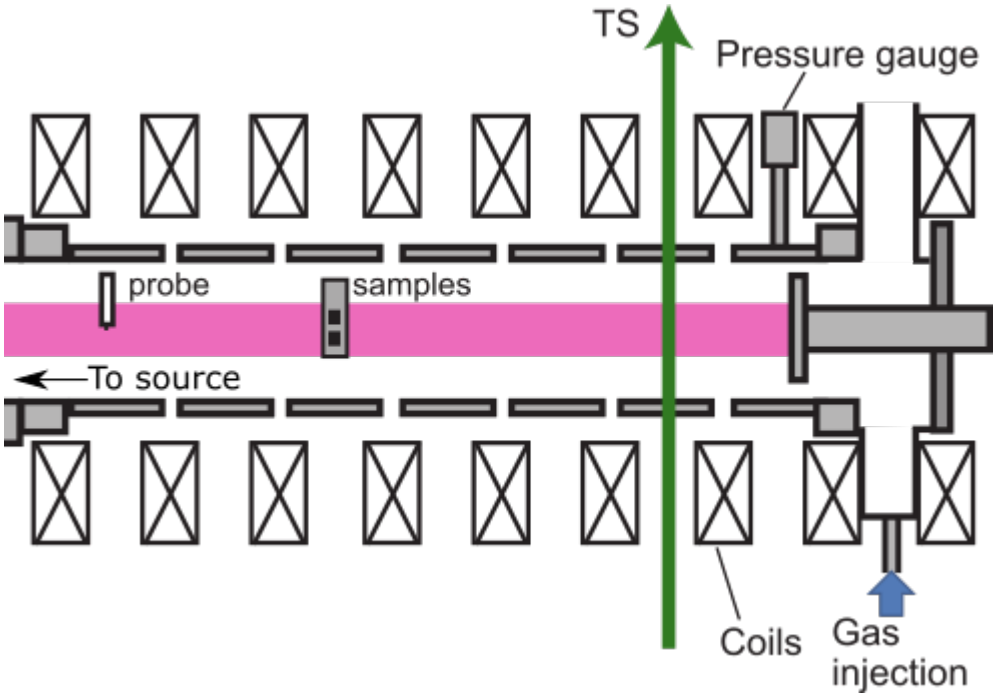

Figure 1: Schematic of the sample region in the NAGDIS-II linear plasma device. The plasma flux and floating potential were calculated using an electrostatic probe located 30 cm upstream from the sample holder.

3. Results and discussion

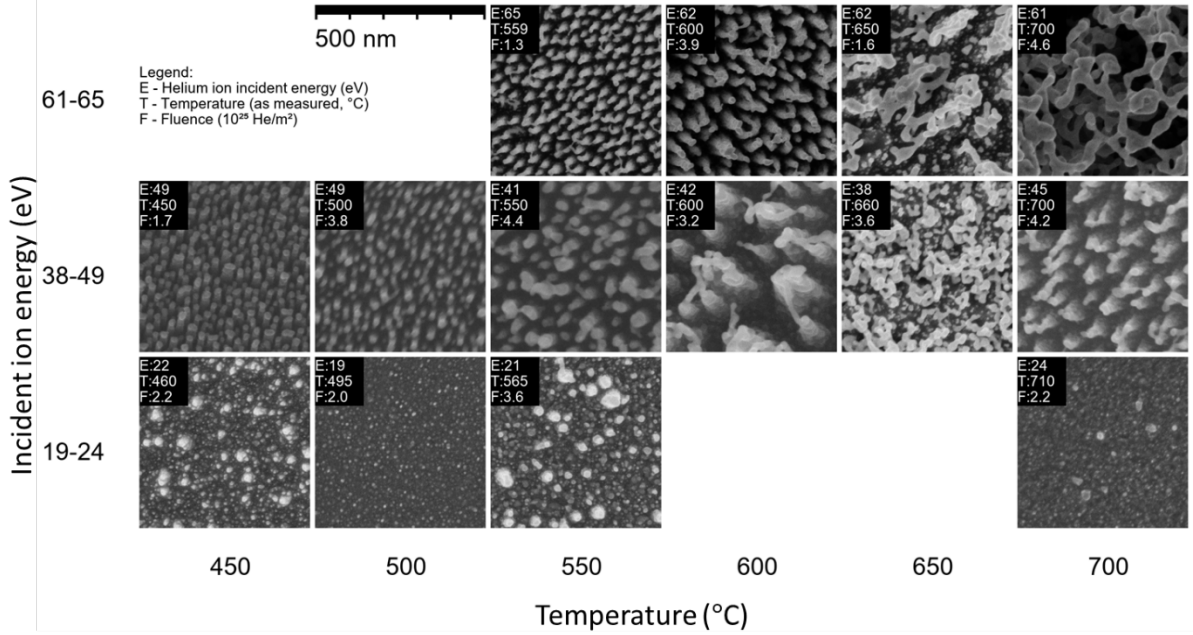

Figure 2: Overview of the surface structures observed on silicon after plasma exposure at varying temperature and incident ion energy. The incident helium ion energy (E), sample temperature (T) and total ion fluence (F) varied somewhat from the target values and are reported in the inset in the top-left of each image.

Figure 2 shows a series of SEM micrographs for each of the exposure conditions that are representative of the sample surfaces. Samples generally exhibited uniform coverage of surface nanostructures, except for a few isolated cases where thermal gradients were present on the sample surface. Nano-structures mostly have a wire-like morphology, with radii that increase from $\sim 10 - 20$ nm at 450 °C to over 100 nm at 600 °C - 650 °C. Conversely, the number density of nanostructures increases with decreasing temperature below 650 °C, with a maximum value of $\sim 7.4 \times 10^{16}\ \mathrm{m}^{-2}$ at 450 °C. The case of a 61 eV ion energy and 700 °C target temperature leads to a unique porous structure of interconnected wires ~10-20 nm in diameter. This porous structure is reminiscent of the "nano-fuzz" structure widely reported in tungsten[18]. At an incident energy of 19-24 eV irregular nanoscale mounds form across all temperatures studied.

Notably, many of the nanostructures reported here differ qualitatively to those reported by Takamura *et al*.[22], which appeared to have a more needle-like morphology possibly due to a greater influence of sputtering on the shaping of nanostructures. By contrast, most of the features observed in this work have a more rounded morphology, or in some cases feature complex branches that cannot be explained by sputtering alone. The reason for this discrepancy is not clear, though it is plausible that differences in the plasma devices used could affect silicon redeposition rates or sputtering from impurity gas species that could account for the differences observed.

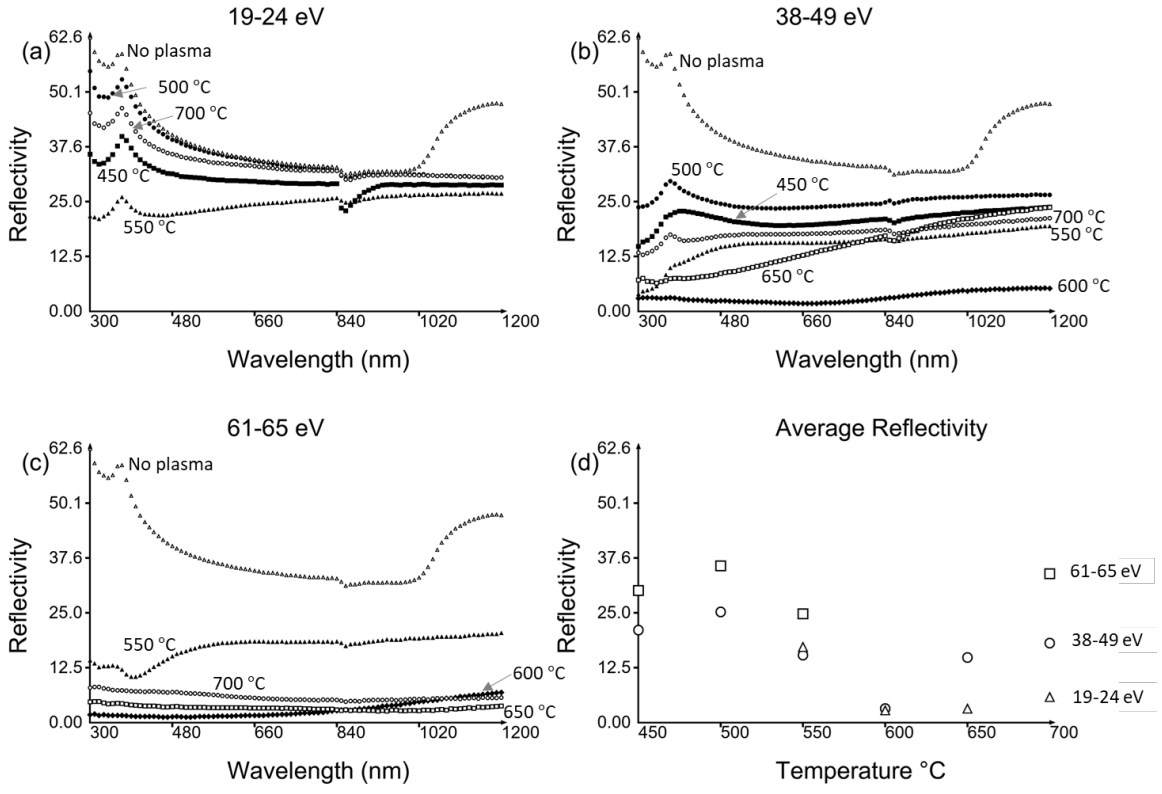

Figure 3: Reflectivity measurements of nanostructured silicon surfaces from 300 nm to 1200 nm for (a) 19-24 eV, (b) 38-49 eV, and (c) 61-65 eV incident helium ion energies. (d) shows the average reflectivity across the measured range for each measurement.

Results from reflectivity measurements for nanostructured silicon are presented in Figure 3. Samples exposed to helium plasma at 19-24 eV incident ion energies showed a more modest average

reduction in reflectivity of around 14-37%, with the most significant reduction observed at 550 °C. At 38-49 eV the reduction in reflectivity of nanostructured surfaces shows a strong dependence on exposure temperature, ranging from only a 36% reduction at 500 °C to almost 92% at 600 °C. Particularly strong suppression was observed for wavelengths below 480 nm. At 600 °C efficient broad-band absorption was observed across the 300-1200 nm wavelength range studied, with surface reflectivity reaching an average value of only 3.2%. This absorption performance is similar to that of silicon exposed to helium plasma at a ~62 eV incident energy at 600 °C and 650 °C (2.9% and 3.3% average reflectivity, respectively). These values are comparable to nanowire silicon solar panel antireflection coatings produced by other methods[29]. For instance, Fang *et al*[30] achieved reflectivity values of 2-3% across the visible spectrum using nanowires growth via wet chemical etching, while the nanowires grown by Zhang *et al*[31] via vapour-liquid-solid epitaxy had reflectivity values on the order of 10%. Reflectivity suppression is also similar to that of Takamura *et al*[22].

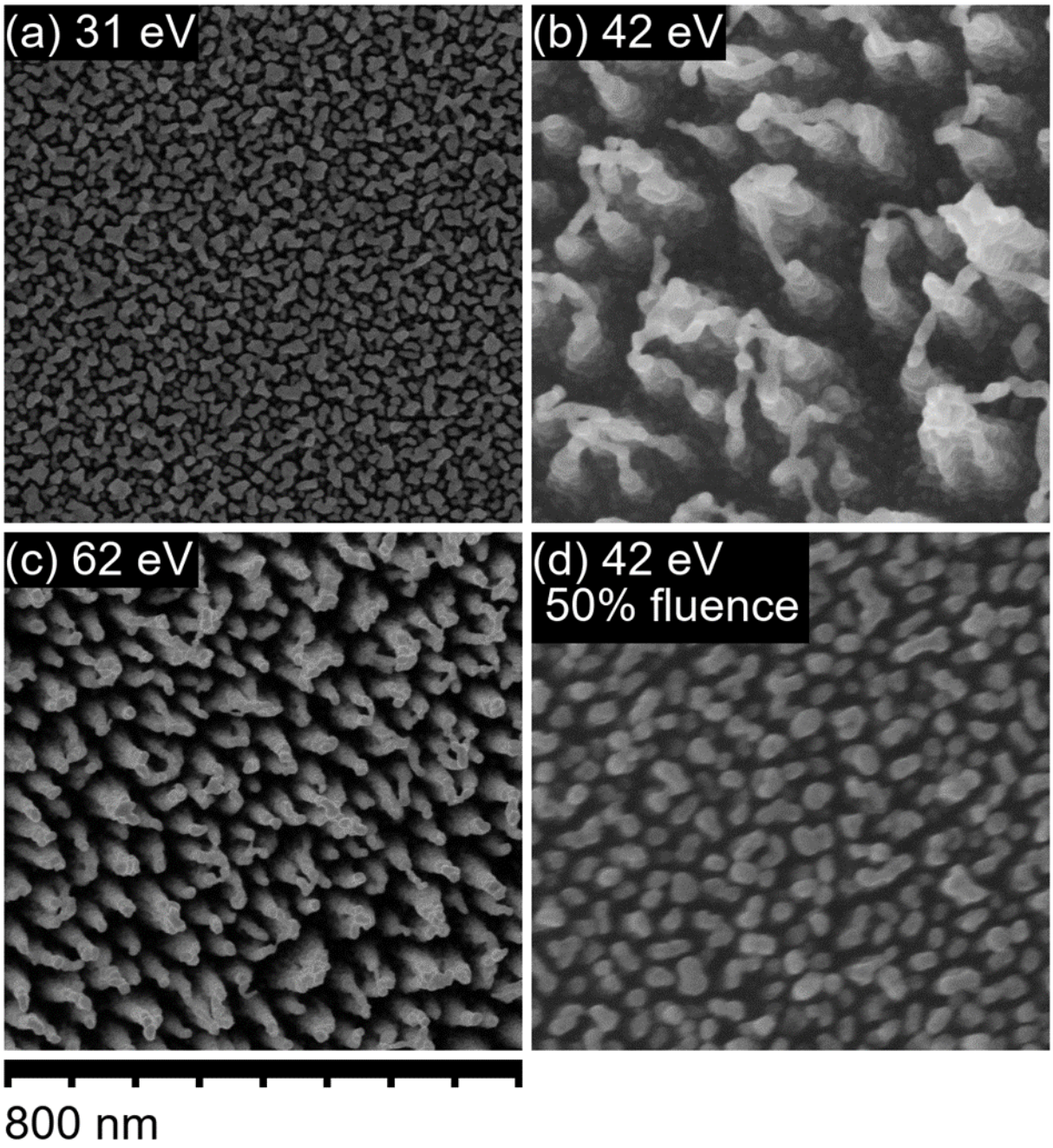

Figure 4: Samples exposed to helium plasma at 600 °C and incident ion energies and fluences of (a) 31 eV and $3.2 \times 10^{25}\mathrm{He} \cdot \mathrm{m}^{-2}$, (b) 42 eV and $3.2 \times 10^{25}\mathrm{He} \cdot \mathrm{m}^{-2}$, (c) 62 eV and $3.9 \times 10^{25}\mathrm{He} \cdot \mathrm{m}^{-2}$, and (d) 42 eV and $1.6 \times 10^{25}\mathrm{He} \cdot \mathrm{m}^{-2}$.

Figure 4 shows the influence of the incident ion energy on the growth of surface nanostructures at 600 °C, which is the optimal temperature for suppressing surface reflectivity. Nanostructure growth occurs for all incident energies studied, with the largest structures occurring for a 42 eV incident ion energy. Monte-Carlo simulations of helium implantation into tungsten predict that at low incident ion energies a significant fraction of incident ions is reflected from the material surface[32], which is consistent with experimental measurements of helium retention[33]. Higher incident energies is expected to reduce surface reflection in silicon as well, thereby enhancing helium sub-surface implantation effects, sputtering and silicon redeposition. The interactions between these effects are not straightforward: while a higher sputtering yield will increase erosion, it will also increase

redeposition, which in turn will increase the number of surface adatoms available for epitaxial growth. Capture of sputtered atoms by nanostructures is known to occur in helium-exposed tungsten[26].

Figure 4 (d) shows the surface of a silicon surface that had been exposed to helium plasma at a 42 eV incident energy, but at half the plasma fluence of Figure 4 (b). The features observed here are very different from those observed at the higher fluence in Figure 4 (b), yet qualitatively similar to those observed for the 31 eV incident energy sample in Figure 4 (a). Growth at 42 eV incident energy appears to initiate with a large number of closely-spaced nucleation sites which eventually agglomerate into the larger, more complex structures observed in Figure 4 (b). Close examination of the morphology of the nanostructures in Figure 4 (b) seems to support this view: nanostructures appear to be circular rods that have become fused together. Some fusing of adjacent nanostructures is also evident for the 62 eV sample in Figure 4 (c).

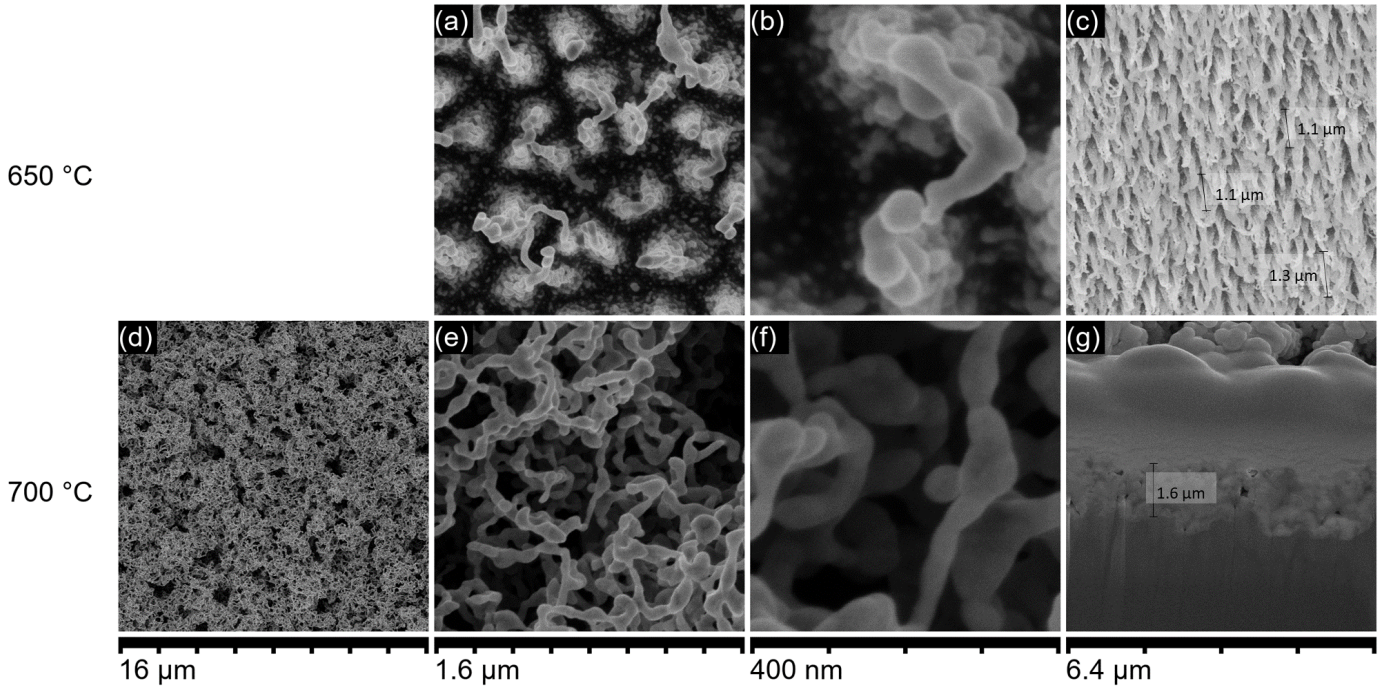

Figure 5: Nanostructure formation under ~62 eV helium ions and substrate temperatures of 650 °C (a-c) and 700 °C (d-f), highlighting features at different scales. (c) The 650 °C sample was imaged at 45 ° to estimate nanostructure length, which was typically $1.1 - 1.3$ µm. (g) A cross sectional image of the 700 °C sample is shown, tilted to 45 °, revealing the depth of the nanostructured layer to be on the order of 1.6 µm.

Close inspection of the nanostructure morphologies provides some insight into their growth dynamics. For 650 °C samples exposed to a He plasma with a ~62 eV incident ion energy (Figure 5 (a,b)) surface features show a stacked terrace configuration. This configuration is consistent with terrace-ledge-kink models of epitaxial growth, where adatom diffusion over the edge of a ledge is suppressed by an Ehrlich-Schwoebel diffusion barrier at the edge[34], biasing the adatom current upwards towards the nanostructure tip. Similar features can also be seen at samples exposed to plasma at 600 °C, as in Figure 4 (b,c). Several protrusions are also observed to bridge adjacent nanostructures together. The protrusions themselves are roughly straight, or display discrete kinks,

indicating crystallographic alignment rather than isotropic growth. These growth characteristics may indicate either stacking faults or twin boundaries[35], or alternatively could come about due to enhanced diffusion along specific crystallographic directions. For instance, anisotropic diffusion occurs along the (100) silicon surface, which is faster parallel to the {110} dimer rows that constitute the surface for this orientation[36], which could plausibly bias growth in those directions. The orientation of most nano-wire bridges is consistent with a {110} diffusion-mediated mechanism.

At 700 °C and a 61 eV implantation energy (Figure 5 (d-f)), nanostructures form a fuzz-like network of fine ~20 nm diameter wires. These structures are similar to the bridging structures at 650 °C, albeit with a greater number of interconnections. The more complex structures observed at 700 °C may indicate a greater degree of surface diffusion along directions which do not contribute significantly to adatom migration at 650 °C, or alternatively, to a greater frequency of stacking faults.

In all samples nanowire spacing is significantly smaller than the wavelength of light used for reflectivity measurements. Thus, to an incident photon the nanowires appear instead as a graded interface with a continuous change in refractive index between air and the silicon substrate, reducing reflection across a broad wavelength range[37]. The thicker the interface region (i.e. longer nanowires), the more effective the material's anti-reflection properties become. The suppression of reflectivity noted in Figure 3 can thus be explained by the emergence of these larger nanostructures. The lengths of the nanostructures were estimated for the samples exposed to >60 eV helium ions at 650 °C by inclining the sample 45°, and at 700 °C via FIB milling and subsequent imaging of the resulting cross section at an incident angle $45°$. The lengths of the resulting nanostructures are typically on the order of ~ 1.2 μm at 650 °C, and 1.6 μm at 700 °C. These nanostructure depths are significantly greater than the $\lambda/4$ requirement for efficient reflection suppression in effective media, and therefore can easily account for the very low reflectivity values across the incident wavelengths studied.

4. Conclusions

Monocrystalline (100) silicon was exposed to high-flux ($7 \times 10^{21} \mathrm{He} \cdot \mathrm{m}^{-2} s^{-1}$ and 2.5×10^{22} He) helium plasma across a range of indicent ion energies and substrate temperatures. Nanostructure formation was observed under all conditions studied, with thicker nanostructure layers forming at higher helium ion incident energies (> 38 eV). The morphology of nanostructures could be controlled by varying the exposure conditions, with dense fields of fine nanowires forming at lower temperatures (< 600 °C), larger irregular nanowires at intermediate temperatures (600 °C – 650 °C), and a porous network structure at 700 °C and an incident ion energy of 61 eV.

Nanowires grown at 600 °C were found to have excellent anti-reflective properties, with broad-band absorption on the order of 2.9-3.2%, similar to other nanowire production methods[29]. This antireflectivity effect occurs due to the fine nanostructured surfaces acting as an effective medium with an apparent graded refractive index, producing a "softer" boundary layer between air and the material substrate.

Acknowledgements

The authors would like to thank Dr H. Chen and the ANU's Centre for Advanced Microscopy for assistance with scanning electron microscopy work, Dr A. Mayon from the ANU's Research School of Engineering for assistance with spectrophotometry measurements, and Dr. H. Dogyun, Ms. S. Feng, and Mr. M. Takagi for their support with experiments on NAGDIS-II. The authors also acknowledge financial support from the Grant-in-Aid for Scientific Research 17KK0132 and 19H01874 from the Japan Society for the Promotion of Science (JSPS).

References

1. Zhang, X. *et al.* Synthesis and characterization of manganese-doped silicon nanoparticles: Bifunctional paramagnetic-optical nanomaterial. *J. Am. Chem. Soc.* **129**, 10668–10669 (2007).

2. Lavorato, G. *et al.* Bifunctional CoFe 2 O 4 /ZnO Core/Shell Nanoparticles for Magnetic Fluid Hyperthermia with Controlled Optical Response. *J. Phys. Chem. C* **122**, 3047–3057 (2018).

3. Shawky, S. M., Awad, A. M., Abugable, A. A. & El-Khamisy, S. F. Gold nanoparticles – An optical biosensor for RNA quantification for cancer and neurologic disorders diagnosis. *Int. J. Nanomedicine* **13**, 8137–8151 (2018).

4. Talapin, D. V., Lee, J.-S., Kovalenko, M. V. & Shevchenko, E. V. Prospects of Colloidal Nanocrystals for Electronic and Optoelectronic Applications. *Chem. Rev.* **110**, 389–458 (2010).

5. Zhang, P., Venkataraman, A. & Papadopoulos, C. Self-assembled gold nanoparticle-molecular electronic networks. *Phys. status solidi* **254**, 1700061 (2017).

6. Li, Y., Li, T., Tian, J., Wang, X. & Cui, H. TiO_2 Nanobelts Decorated with In_2S_3 Nanoparticles as Photocatalysts with Enhanced Full-Solar-Spectrum (UV-vis-NIR) Photocatalytic Activity toward the Degradation of Tetracycline. *Part. Part. Syst. Charact.* **34**, 1700127 (2017).

7. Sood, S., Umar, A., Mehta, S. K. & Kansal, S. K. Highly effective Fe-doped TiO2 nanoparticles photocatalysts for visible-light driven photocatalytic degradation of toxic organic compounds. *J. Colloid Interface Sci.* **450**, 213–223 (2015).

8. Wu, D. *et al.* $Co(OH)_2$ Nanoparticle-Encapsulating Conductive Nanowires Array: Room-Temperature Electrochemical Preparation for High-Performance Water Oxidation Electrocatalysis. *Adv. Mater.* **30**, 1705366 (2018).

9. Kim, S. H., Park, B. C., Jeon, Y. S. & Kim, Y. K. MnO2 Nanowire-CeO2 Nanoparticle Composite Catalysts for the Selective Catalytic Reduction of NO x with NH3. *ACS Appl. Mater. Interfaces* **10**, 32112–32119 (2018).

10. Ren, Y., Ma, Z. & Bruce, P. G. Ordered mesoporous metal oxides: synthesis and applications. *Chem. Soc. Rev.* **41**, 4909 (2012).

11. Jia, X. *et al.* Hydrophilic Fe 3 O 4 nanoparticles prepared by ferrocene as high-efficiency heterogeneous Fenton catalyst for the degradation of methyl orange. *Appl. Organomet. Chem.* **33**, e4826 (2019).

12. Lu, Y., Jiang, Y., Gao, X., Wang, X. & Chen, W. Highly Active and Durable PdAg@Pd Core-Shell Nanoparticles as Fuel-Cell Electrocatalysts for the Oxygen Reduction Reaction. *Part. Part. Syst. Charact.* **33**, 560–568 (2016).

13. Shen, T. *et al.* Rationally Designed Silicon Nanostructures as Anode Material for Lithium-Ion Batteries. *Adv. Eng. Mater.* **20**, 1700591 (2018).

14. Kim, J. H., Mirzaei, A., Kim, H. W. & Kim, S. S. Extremely sensitive and selective sub-ppm CO detection by the synergistic effect of Au nanoparticles and core–shell nanowires. *Sensors Actuators, B Chem.* **249**, 177–188 (2017).

15. Park, H. & Kim, C. Analysis of diffuse reflectivity of a highly disordered GaN nanostructure as an antireflection coating. *Opt. Lett.* **37**, 611 (2012).

16. Perl, E. E., McMahon, W. E., Bowers, J. E. & Friedman, D. J. Design of antireflective nanostructures and optical coatings for next-generation multijunction photovoltaic devices. *Opt. Express* **22**, A1243 (2014).

17. Xia, B., Wang, B., Chen, Z., Zhang, Q. & Shi, J. Drug Delivery: Near-Infrared Light-Triggered Intracellular Delivery of Anticancer Drugs Using Porous Silicon Nanoparticles Conjugated with IR820 Dyes (Adv. Mater. Interfaces 4/2016). *Adv. Mater. Interfaces* **3**, n/a-n/a (2016).

18. TAKAMURA, S., OHNO, N., NISHIJIMA, D. & KAJITA, S. Formation of Nanostructured Tungsten with Arborescent Shape due to Helium Plasma Irradiation. *Plasma Fusion Res.* **1**, 51 (2006).

19. Kajita, S., Kawaguchi, S., Ohno, N. & Yoshida, N. Enhanced growth of large-scale nanostructures with metallic ion precipitation in helium plasmas. *Sci. Rep.* **8**, 56 (2018).

20. Kajita, S. *et al.* Fuzzy nanostructure growth on precious metals by He plasma irradiation. *Surf. Coatings Technol.* **340**, 86–92 (2018).

21. Takamura, S. *et al.* Nanostructure formation on silicon surfaces by using low energy helium plasma exposure. *Jpn. J. Appl. Phys.* **55**, 120301 (2016).

22. Takamura, S. *et al.* Black silicon with nanostructured surface formed by low energy helium plasma irradiation. *Appl. Surf. Sci.* **487**, 755–765 (2019).

23. Thompson, M., Magyar, L. & Corr, C. Nanoscale modification of silicon and germanium surfaces exposed to low-energy helium plasma. *Sci. Rep.* **9**, 1–9 (2019).

24. Doerner, R. P. *et al.* Investigation of He-W interactions using DiMES on DIII-D. in *Physica Scripta* vol. 2016 (2016).

25. Baldwin, M. J. & Doerner, R. P. Formation of helium induced nanostructure 'fuzz' on various tungsten grades. *J. Nucl. Mater.* **404**, 165–173 (2010).

26. Nishijima, D., Baldwin, M. J., Doerner, R. P. & Yu, J. H. Sputtering properties of tungsten 'fuzzy' surfaces. *J. Nucl. Mater.* **415**, S96–S99 (2011).

27. Ohno, N. *et al.* Static and dynamic behaviour of plasma detachment in the divertor simulator experiment NAGDIS-II. *Nucl. Fusion* **41**, 1055–1065 (2001).

28. Schneider, C. A., Rasband, W. S. & Eliceiri, K. W. NIH Image to ImageJ: 25 years of image analysis. *Nature Methods* vol. 9 671–675 (2012).

29. Sahoo, M. K. & Kale, P. Integration of silicon nanowires in solar cell structure for efficiency enhancement: A review. *Journal of Materiomics* vol. 5 34–48 (2019).

30. Fang, H., Li, X., Song, S., Xu, Y. & Zhu, J. Fabrication of slantingly-aligned silicon nanowire arrays for solar cell applications. *Nanotechnology* **19**, (2008).

31. Zhang, P. *et al.* Dense nanoimprinted silicon nanowire arrays with passivated axial p-i-n junctions for photovoltaic applications. *J. Appl. Phys.* **117**, 125104 (2015).

32. Borovikov, V., Voter, A. F. & Tang, X.-Z. Reflection and implantation of low energy helium with tungsten surfaces. *J. Nucl. Mater.* **447**, 254–270 (2014).

33. Thompson, M. *et al.* Observation of a helium ion energy threshold for retention in tungsten exposed to hydrogen/helium mixture plasma. *Nucl. Fusion* **56**, 104002 (2016).

34. Rusponi, S., Costantini, G., Boragno, C. & Valbusa, U. Ripple Wave Vector Rotation in Anisotropic Crystal Sputtering. (1998).

35. He, Z., Nguyen, H. T., Duc Toan, L. & Pribat, D. A detailed study of kinking in indium-catalyzed silicon nanowires. *CrystEngComm* **17**, 6286–6296 (2015).

36. Mo, Y. W., Kleiner, J., Webb, M. B. & Lagally, M. G. Surface self-diffusion of Si on Si(001). *Surf.*

Sci. **268**, 275–295 (1992).

37. Saini, S. K. & Nair, R. V. Quantitative analysis of gradient effective refractive index in silicon nanowires for broadband light trapping and anti-reflective properties. *J. Appl. Phys.* **125**, 103102 (2019).